SANDIA REPORT
SAND2015-8758
Unlimited Release
September 2015

Quantitative Imaging of Turbulent Mixing Dynamics in High-Pressure Fuel Injection to Enable Predictive Simulations of Engine Combustion

Jonathan H. Frank, Lyle M. Pickett, Scott E. Bisson, Brian D. Patterson, Adam J. Ruggles, Scott A. Skeen, Julien Manin, Erxiong Huang, Dave J. Cicone, Panos Sphicas

Prepared by
Sandia National Laboratories
Albuquerque, New Mexico 87185 and Livermore, California 94550

Sandia National Laboratories is a multi-program laboratory managed and operated by Sandia Corporation,
a wholly owned subsidiary of Lockheed Martin Corporation, for the U.S. Department of Energy's
National Nuclear Security Administration under contract DE-AC04-94AL85000.

Sandia National Laboratories

Issued by Sandia National Laboratories, operated for the United States Department of Energy by Sandia Corporation.

Available to DOE and DOE contractors from
U.S. Department of Energy
Office of Scientific and Technical Information
P.O. Box 62
Oak Ridge, TN 37831

Telephone: (865) 576-8401
Facsimile: (865) 576-5728
E-Mail: reports@osti.gov
Online ordering: http://www.osti.gov/scitech

Available to the public from
U.S. Department of Commerce
National Technical Information Service
5301 Shawnee Rd
Alexandria, VA 22312

Telephone: (800) 553-6847
Facsimile: (703) 605-6900
E-Mail: orders@ntis.gov
Online order: http://www.ntis.gov/search

SAND2015-8758
Unlimited Release
September 2015

Quantitative Imaging of Turbulent Mixing Dynamics in High-Pressure Fuel Injection to Enable Predictive Simulations of Engine Combustion

Jonathan H. Frank[1], Lyle M. Pickett[2], Scott E. Bisson[3], Brian D. Patterson[4], Adam J. Ruggles[1],
Scott A. Skeen[2], Julien Manin[2], Erxiong Huang[1], Dave J. Cicone[2], Panos Sphicas[2]

[1]Reacting Flows Dept., [2]Engine Combustion Dept.,
[3]Remote Sensing and Energetic Materials Dept., [4]Combustion Chemistry Dept.
Sandia National Laboratories
P.O. Box 969
Livermore, California 94551-MS9051

Abstract

In this LDRD project, we developed a capability for quantitative high-speed imaging measurements of high-pressure fuel injection dynamics to advance understanding of turbulent mixing in transcritical flows, ignition, and flame stabilization mechanisms, and to provide essential validation data for developing predictive tools for engine combustion simulations. Advanced, fuel-efficient engine technologies rely on fuel injection into a high-pressure, high-temperature environment for mixture preparation and combustion. However, the dynamics of fuel injection are not well understood and pose significant experimental and modeling challenges. To address the need for quantitative high-speed measurements, we developed a Nd:YAG laser that provides a 5ms burst of pulses at 100kHz on a robust mobile platform. Using this laser, we demonstrated spatially and temporally resolved Rayleigh scattering imaging and particle image velocimetry measurements of turbulent mixing in high-pressure gas-phase flows and vaporizing sprays. Quantitative interpretation of high-pressure measurements was advanced by reducing and correcting interferences and imaging artifacts.

CONTENTS

FIGURES

TABLES

1. INTRODUCTION

The development and application of high-fidelity imaging diagnostics for understanding fuel injection dynamics is a potentially high-impact research area given the continually increasing demand for improved fuel efficiency and reduced emissions over a wide range of operating conditions. In this LDRD project, we have developed a capability for quantitative imaging measurements of high-pressure fuel injection dynamics to advance our understanding of turbulent mixing in transcritical flows, ignition, and flame stabilization mechanisms, and to provide essential validation data for developing predictive tools for engine combustion simulations. Advanced, fuel-efficient engine technologies rely on fuel injection into a high-pressure, high-temperature environment for mixture preparation and combustion. Fuel injection conditions can span thermodynamic critical conditions, which affects the fuel spray atomization process. At subcritical conditions, surface tension provides a distinct liquid-gas interface. However, at supercritical conditions this interface becomes diffuse and the injected fuel forms a jet of dense fluid without a distinct phase transition. It is currently unknown how the different physical properties of subcritical and supercritical sprays affect turbulent fuel mixing dynamics. The dynamics of fuel mixing and combustion are not well understood and cannot be accurately predicted.

Quantitative measurements for model validation are lacking because spatially and temporally resolved measurements of turbulent mixing and combustion dynamics in multi-phase, high-pressure, high-temperature flows pose significant diagnostic challenges. Advanced diagnostics development at engine pressures and temperatures are needed to enable quantitative high-resolution measurements of the temporal evolution of fuel injection. The ability to perform these high-fidelity measurements will transform our understanding of fuel injection dynamics, which affect engine combustion processes such as flame lift-off, soot formation, and cycle-to-cycle variations. These quantitative data will be used for testing turbulent mixing models that are central to Sandia's efforts to develop predictive simulations of fuel injection.

Previous capabilities for imaging measurements of fuel injection in Sandia's constant-volume high-pressure spray injection facility were limited to single-shot planar laser imaging, which cannot probe injection dynamics, and high-repetition rate line-of-sight techniques such as Schlieren, shadowgraphs, or chemiluminescence imaging, which have insufficient spatial resolution since they are path-integrated measurements. Imaging diagnostic techniques using laser light scattering provide high-resolution, non-intrusive measurements of turbulent flows. However, their implementation at the requisite repetition rates and at engine relevant conditions is particularly challenging. We address these challenges by innovative laser diagnostic approaches, including the construction of a custom pulse-burst laser system, which provides a short burst of pulses at repetition rates needed for following the motion of high-speed flows while minimizing the size, cost, and thermal loading. A continuous stream of laser pulses is not needed since high repetition rate imaging is required only during the injection event, which lasts on the order of milliseconds.

This report describes the development of the mobile pulse-burst laser system in Section 2 followed by a demonstration of our newly developed method to correct for the severe laser beam-steering artifacts in high-pressure Rayleigh scattering measurements in Section 3. In

Section 4, the combination of the pulse-burst laser and beam-steering corrections are applied to 100 kHz Rayleigh scattering measurements of the temporal evolution of high-pressure transient gas-phase jets. In Section 5, we demonstrate 100 kHz scalar and velocity imaging of turbulent mixing in Sandia's constant-volume high-pressure spray injection facility at engine relevant conditions using Rayleigh scattering and particle image velocimetry (PIV).

2. PULSE-BURST LASER DEVELOPMENT

2.1. Design Considerations

The advancement of high-speed imaging capabilities will provide new insights into critical regimes of turbulent combustion. To access this new frontier, we have embarked on the development of a high rep-rate burst mode laser, fabricated in part from custom commercial diode-pumped Nd:YAG laser modules. The basic specifications of the proposed system are summarized below:

1. 100 kHz rep-rate
2. burst width – 5 ms
3. individual pulse width ~ 5-10 ns
4. single pulse energy ~ 50-100 mJ @1064 nm
5. output wavelength(s) 532 nm, 355 nm
6. fit onto portable breadboard approximately 4 X 6 ft

In this work, we have selected Nd:YAG as the lasing medium since it is ubiquitous in the industry, high energy is easily obtainable and scalable, modular design is facilitated. However, YAG exhibits strong thermal lensing and birefringence under high-energy conditions, which ultimately leads to severe beam degradation through focusing, polarization distortion and potentially damage. To mitigate this, we have chosen to operate the burst at a rate equal to or less than 1 burst per second. Furthermore, the burst width is restricted to 5 ms or less. Under these conditions, it is possible to have consistent performance over the burst envelope.

A quick calculation illuminates the daunting challenge of this effort –a 5 ms burst at 100 kHz and 50 mJ, requires an extracted energy of 25 J! The actual energy delivered to the gain medium is many times greater than this energy. While the single pulse energy is extremely modest and achievable by small low cost systems, operation in burst mode poses many challenges including the requirement for high pump power and thermal mitigation. With these considerations in mind, the design strategy becomes clearer although challenges remain. Given the choice of Nd:YAG as the lasing medium, there is the question of flashlamp or diode pumping. Flashlamp pumping is commonly employed in low rep-rate (i.e. 10 Hz) systems with high energy and is low cost. However, flashlamp pumping delivers significant excess heat load due to the broadband nature of the lamp. Furthermore, it is not easily amenable to pumping over a 5 ms window. In contrast, diode pumping significantly reduces excess thermal loading by pumping at a wavelength of 808 nm, not far from the lasing wavelength of 1064 nm, which reduces the excess heat input. In addition, diode pumping is easily amenable to long pumping times. The only major drawback of diode pumping is the relatively low spectral brightness compared to a flashlamp. Thus, large diode arrays are required to meet the pump requirements. Given the high rep-rate and that the inter-pulse period is significantly shorter than the upper state lifetime, it is expected that the stage gain will be low, thus requiring more stages than a typical amplifier chain. A final consideration is the seed laser. Two approaches are possible, a switched cw laser yielding very low energies per pulse (i.e. nJ), or a high rep-rate pulsed commercial microJoule level laser. The choice of seed does affect the overall system gain requirement.

As there is considerable technical risk, we have attempted to reduce risk through the use of proven, commercial diode pumped laser technology that can be modified to meet performance requirements. A scalable modular design is also employed to reduce requirements in any one stage. Much of the design considerations can be found in Koechner (*1*).

2.2. Design Architecture

The starting point of the system is based on a commercial, high rep-rate, multi-mode Q-switched laser manufactured by Spectra-Physics. The basic laser emits approximately 20-30 μJ at 100 kHz in an 8 ns pulse. Thus, for an output of 100 mJ per pulse an overall system gain of approximately 5000 is required. This can be achieved in three stages, with stage gains of approximately 10-20 for the first two stages followed by lower gains for the final stage. To achieve these gains, we employ two or four -pass amplifiers with all passive elements. A passive switching architecture is used since at a 100 kHz rep-rate it would be difficult to switch pulses in and out of an amplifier. The amplifier modules are based on Cutting Edge Optronics (Northrop Grumman) diode-pumped, Nd:YAG rod modules, modified to accommodate the higher pump rates required. To reduce risk, we decided to run parallel amplifiers in the final stage to achieve two beamlines of 50 mJ per pulse each, rather than a single beamline of 100 mJ. Figure 1 illustrates the basic system design. A relay-imaged design was considered, but long focal length lenses were required to maintain a uniform image in the YAG rods making the system size impractical. Instead, the seed beam propagates through the first 2 mm diameter YAG rod, which is then resized for the 5 mm YAG rod followed by relay imaging/spatial filtering into the final two 1 cm diameter YAG heads. Since the amplifiers are operated in a saturated regime the beam acquires a near top hat profile. Throughout the system we use Faraday rotators to achieve passive switching in either 2 or 4 pass configurations. This would also be possible with quarter wave plates, however thermal birefringence can only be compensated with Faraday rotators. Any thermal birefringence would certainly degrade performance, especially harmonic conversion since it is highly polarization dependent. The following describes the system stages.

Seed Laser

The seed laser is based on a variable rep-rate Q switched Spectra-Physics laser operated at 100 kHz and 25 μJ per pulse in approximately 8 ns. We operate the laser at less than 1 Hz rep-rate in a 5 ms super pulse. This laser is multi-mode, which produces significant amplitude modulation in the pulse. Ultimately, this was a problem for injection into a fiber-based preamplifier. The beam profile was approximately Gaussian. The laser was very susceptible to feedback so a Faraday isolator was used to isolate the laser from potential feedback. Without the isolator, pulse instabilities were observed at higher upstream pulse energies.

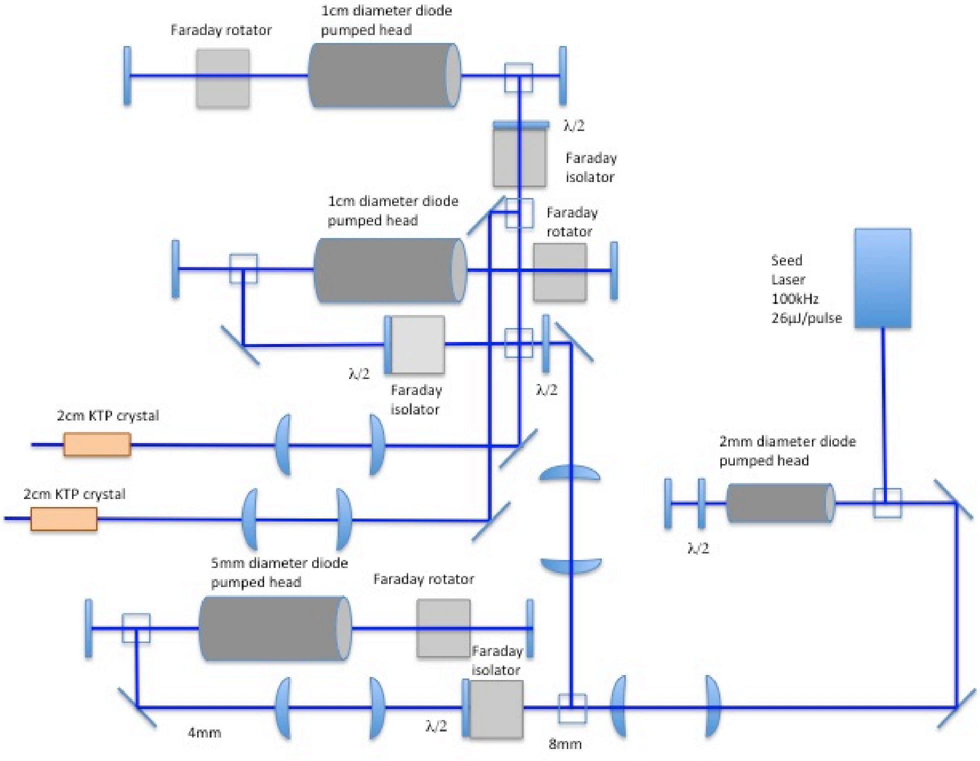

Figure 1. Schematic of the burst mode laser. To reduce technical risk, the architecture employs two beamlines on the final leg. Ultimately, the two 1 cm diameter rods could be employed in a 4-pass followed by a 2-pass configuration. Account must also be taken for thermal effects, even for a 1 Hz burst period.

Preamp

Initially, we selected a pulsed, large mode area fiber laser for amplification of the seed up to the 500 µJ to 1 mJ level. However, this approach suffered from numerous challenges that forced a design change from a fiber laser to a commercial diode-pumped head. For completeness, we review the highlights of this effort and illustrate the problems faced with a fiber-based system. During the course of this effort, a number of architectures were investigated all plagued with parasitic nonlinear effects. Figure 2 shows a schematic of one of the fiber based architectures. A photo of the seed laser with isolation stages and a large mode area fiber amplifier (on wooden spools) is shown below in Figure 3.

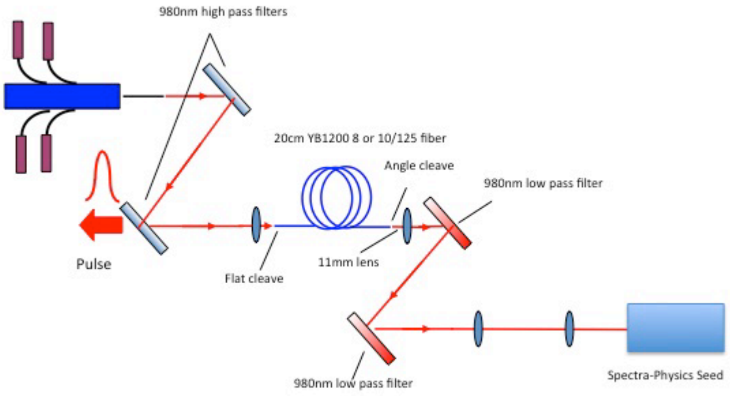

Figure 2. Simplified schematic of the fiber based seed preamplifier. Numerous designs were investigated but all were plagued by parasitic nonlinearities such as self-phase modulation.

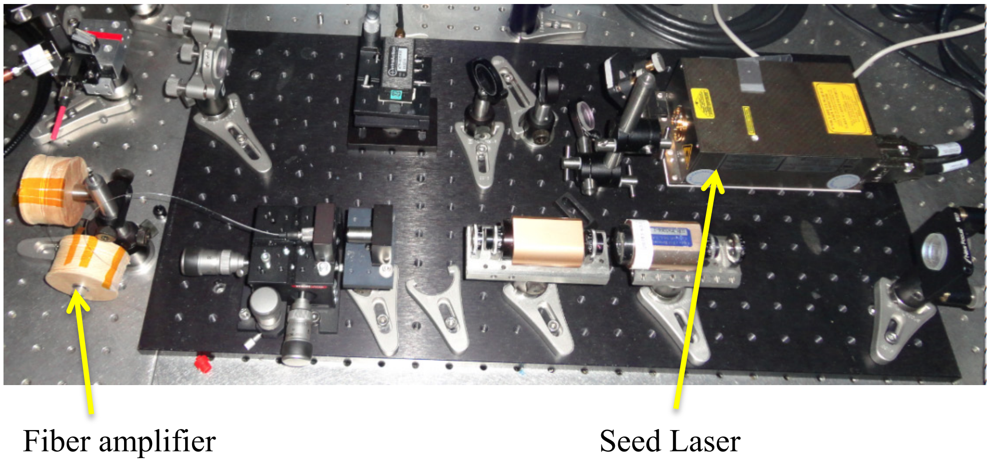

Figure 3. Photograph of the seed laser integrated with the fiber amplifier. The fiber amplifier is based on a large mode area fiber which was coiled in two dimensions (on wooden spools) to produce a truly single spatial mode beam.

While the fiber based preamp could deliver sufficient energy (> 200 μJ – 1 mJ) to drive the subsequent amplifiers, self-phase modulation broadened the spectral output beyond the bandwidth of Nd:YAG, limiting the achievable gain (Figure 4). This could be partly mitigated by a combination of shortening the fiber, increasing the mode area or increasing the seed pulse length (Figure 5). Unfortunately, the seed laser parameters such as pulse length could not be varied. The production of self-phase modulation was probably further exacerbated by mode beating in the seed pulse. Even if a single mode seed were available for this effort, the narrow bandwidth would enhance other nonlinear effects such as stimulated Brillouin scattering (SBS). For these reasons, a fiber based preamp approach was abandoned in favor of a small diameter (2 mm) diode pumped Nd:YAG head.

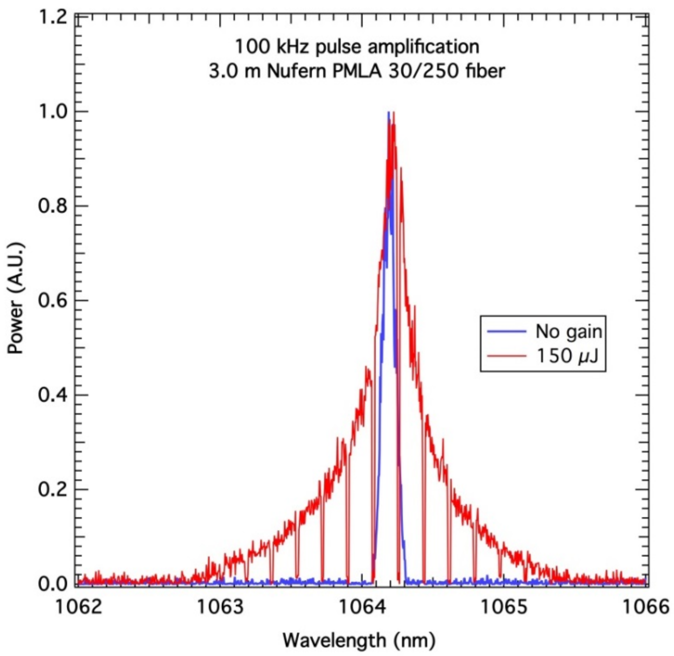

Figure 4. Measurement of the spectral output of the preamp, with (red curve) and without pumping (blue curve). Even at modest output energies of 150μJ, the output bandwidth is increased substantially over that of the input. The vertical structure in the amplified pulse (shown in red) is an instrumental artifact.

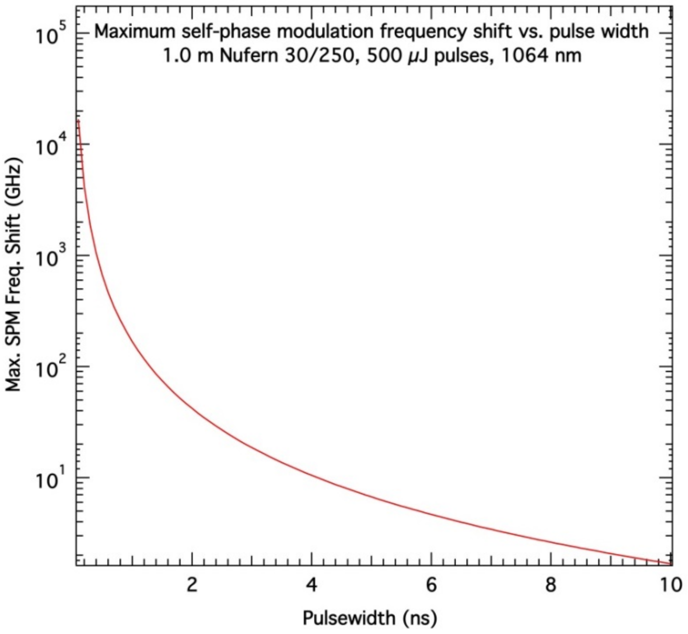

Figure 5. Calculated self-phase modulation (SPM) induced bandwidth increase. The dependence on pulse width is strong, favoring longer pulses widths. The multi-mode structure of the seed laser would likely enhance this effect. Ultimately SPM can increase the bandwidth beyond the gain bandwidth of Nd:YAG. The calculation is based on fiber parameters used in this work (refer to figure legend).

2 mm diode pumped Nd:YAG head

As an alternative to the fiber amplifier, we employed a commercial 2 mm diameter diode pumped Nd:YAG head manufactured by Northrop Grumman (model RBAT24). The output from the seed laser (100 kHz, 8 ns, 25 μJ pulses) is amplified in a two-pass configuration, yielding outputs in the range of 300-450 μJ/pulse, depending on pump power. The amplifier is pumped by 12 diode laser bars at approximately 50 W continuous wave power. The rod is 73 mm long by 2 mm in diameter and doped over a 40 mm region at 0.7% by weight. We operate the amplifier in a pulsed mode, with 70 amps of current in a 5 ms long pulse. Table 1 summarizes the amplifier performance for various diode currents and amplifier configurations, single or double pass. Ultimately, we achieve an output that is sufficient to fully saturate the next stage. The input beam from the seed laser is reformatted to approximately 1 mm diameter for the 2 mm rod amp but is not spatially filtered. After two passes in the rod amp, pumped at 70A, the beam has the profile shown in Figure 6.

Table 1. 2 mm head performance

RBAT 24 : 2mm Diameter Nd:YAG Rod			
Pump Current (A)	Single Pass (uJ)	Double Pass (uJ)	
30	29.3	46.7	
35	37.3	72.8	
40	49	106	
45	61.3	151	
50	76.2	200	
55	92.7	257	
60	111	318	
65	132	387	
68	144	429	
70	154	456	

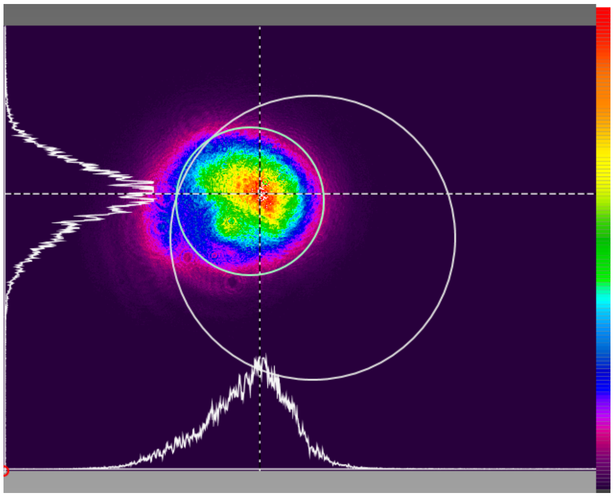

Figure 6. Beam profile after two passes in the 2 mm rod amp operated at full pump power (70A).

5 mm diode pumped Nd:YAG head
Specifications
The output from the 2 mm head is further amplified in a four-pass, 5 mm diameter amplifier head. This head employs a 5 mm diameter, 167mm long Nd:YAG rod doped at 0.7% over the interior 100 mm of the rod. The outer ends of the rod are undoped and serve to reduce thermally induced mechanical stress. Since we require more pump energy than the standard design, the rod is pumped with 50 diode bars, grouped into five arrays with ten diodes each surrounding the rod. Each diode bar emits approximately 60 W at 65 amps of drive current at 808 nm, the peak absorption of Nd:YAG. At the full pump power of 3 kW, the total energy delivered to the rod can be nearly 15 J. Figure 7 illustrates the 5 mm and 10 mm amplifier coupled in a four pass configuration. This was an early breadboard layout but clearly shows the basic architecture.

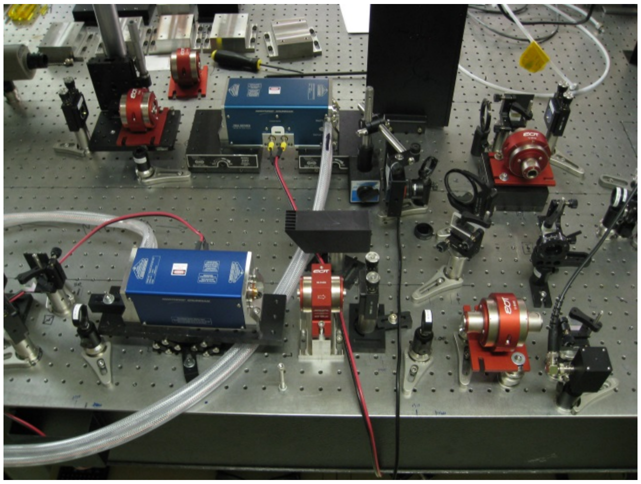

Figure 7. Photograph of the 5 mm (foreground) and 10 mm (background) four-pass amplifiers (blue heads). The red components are either Faraday rotators (short) or isolators (long).

Performance
The performance of the system is basically set by two parameters – the small signal gain and the saturation fluence, which for YAG is 0.67 J/cm^2. A full three-dimensional model is beyond the scope of this work, but basic performance can be predicted with a modified Frantz-Nodvik analysis (*2*). The performance of this stage is tabulated below in Table 2. For comparison, model performance is included for the case of driving the diodes at 65 amps. Agreement is generally good although the model slightly over predicts performance. At present, no account is made for diffraction or scattering losses, which may account for some of the disagreement.

The input beam is formatted for an approximately 90% fill factor without gain. However the fill factor becomes nearly 100% when the amplifier is operated in saturation. While this is efficient, rod edge diffraction effects can be quite pronounced making propagation of the beam difficult. The gain may seem low but it must be emphasized that this is in burst mode with 10 μs between pulses. Thus, there is little time to replenish the extracted energy between pulses. It should be noted that initially, performance was well below expectations at high rep-rates but satisfactory for single pulse amplification. This was ultimately identified as a defect in the diode laser bars that were manufactured to operate at the absorption minimum of YAG. Figure 8 illustrates the diode output overlaid with the Nd:YAG absorption. This defect was resolved by fabricating new diode arrays that were optimized for operation at the peak Nd:YAG absorption. Unfortunately, this delayed the project by three months. Overall, the amplification of the beam produced a top-hat like beam with clear diffraction present but with only a central bright spot and outer ring (Figure 9). This is in contrast to the Gaussian like input beam, indicating saturation in the amplifier.

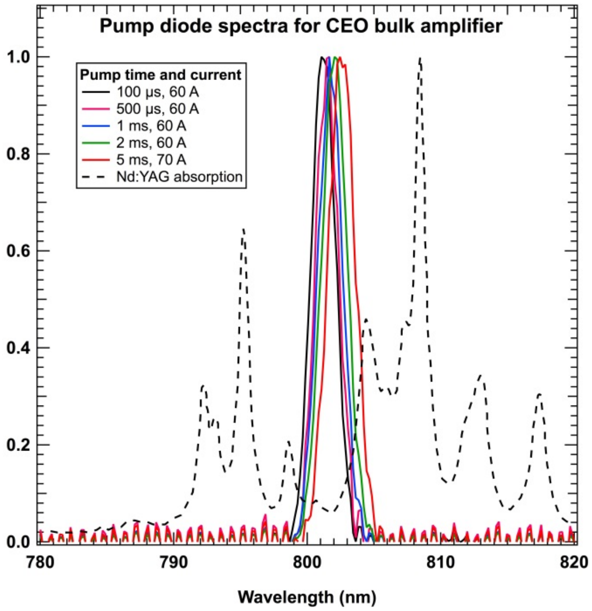

Figure 8. Pump diode wavelength overlaid with the absorption spectrum of Nd:YAG. These diodes were incorrectly manufactured at the absorption minimum at 802 nm and could not be tuned to the absorption peak. This was resolved by fabricating new pump diodes that were optimized for operation at the peak Nd:YAG absorption.

Table 2. 5 mm head measured performance

REA 5010 : 5mm Diameter Nd:YAG Rod			
Pump Current (A)	Single Pass (mJ)	Double Pass (mJ)	Four Pass (mJ)
0	0.362		
30	0.773	1.19	1.81
35	0.955	1.59	2.47
40	1.17	2.07	3.23
45	1.43	2.63	4.07
50	1.74	3.27	4.99
55	2.07	3.96	5.97
60	2.43	4.74	7.02
65	2.84 (2.5mJ model)	5.46 (5.8mJ model)	8.02 (8.8mJ model)
70	3.25	6.15	9.03

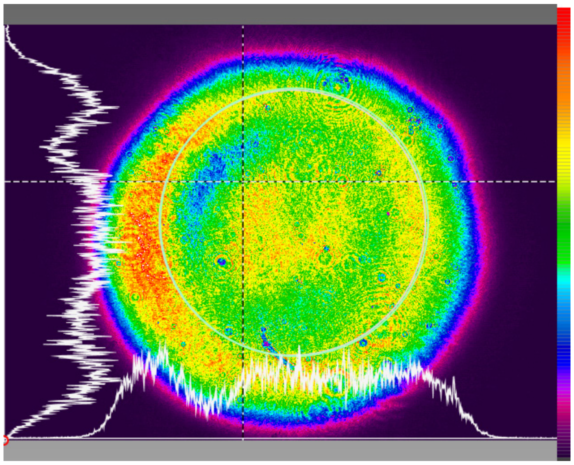

Figure 9. Image of the beam after four passes in the 5 mm rod amp at full pump power (70A). In contrast to the output of the 2 mm rod, the beam profile is more flattened due to operation in the saturation regime. Diffraction is also present as a central spot with an outer ring.

10 mm diode pumped Nd:YAG heads

The output from the 5 mm rod amp is further amplified in two, 10 mm diameter heads, in parallel. This architecture was chosen for risk reduction but could easily be modified for two 10 mm amps in series. The rods in these heads are 188 mm long with an active (doped) length of 120 mm. The rod is pumped by 140 diode bars arranged in five arrays, each with 28 bars. In contrast to the 5 mm head, these diodes are mounted transversely to the rod axis to reduce pump imprinting on the amplified beam. At 65A of pump current, each diode bar emits approximately 60 W/bar. In the present configuration, each amp receives approximately one half of the output from the 5 mm head, which is reformatted to fill the head. Some inter-stage spatial filtering is used to provide beam cleanup between the output of the 5 mm head and input to the two 10 mm heads. Table 3 summarizes the performance with approximately 4 mJ/pulse input. At full pump power (70A), the output is 36.8 mJ, although outputs of up to 40mJ have been observed. This is in contrast to the predicted value of approximately 50 mJ/pulse. Note that with four passes, the amplifier is highly saturated. This also suggests that a configuration of two, 2-pass amplifiers in series would produce 70-80 mJ of output in a single beamline. It is important to point out that amplified spontaneous emission (ASE) is not an issue since the system gain is low. This is due to the short repumping time between pulses. However, special care must be taken with injection of the first pulse. The timing of the pump diodes is such that the diodes are just turning on during injection of the first pulse. If the diodes were turned on earlier, there is risk that the first pulse could build to very high energies and damage the system. Furthermore, the diode temperature is adjusted to achieve a relatively flat amplification profile over the pulse burst (Figure 10). This is necessary since the diode wavelength tunes with temperature (approximately 0.3 nm/°C). We have also found that for rep rates greater than 1 Hz, thermal lensing in the YAG rods is evident and re-optimization (beam formatting) of the system is necessary, especially into the harmonic conversion crystals. Although the focal lengths of the thermal lenses were on the order of 8 m, when passed through an amplifier head four times, high intensity focal spots could be present on the optical breadboard, posing a damage threat. Although the beam is spatially filtered between the 5 mm and 10 mm heads, diffraction is also present on the output beam but at a higher spatial frequency (Figure 11). The final system configuration with all heads is shown below in Figure 12.

Table 3. Measured performance of the 10mm diameter head

REA 10012 : 10mm Diameter Nd:YAG Rod			
Pump Current (A)	Single Pass (mJ)	Double Pass (mJ)	Four Pass (mJ)
0	3.33		
30	6.62	9	9.39
35	7.88	11.33	12.21
40	9.32	13.95	15.31
45	10.81	17.11	18.89
50	12.41	20.11	22.34
55	14.2	23.35	25.91
60	15.96	26.55	29.44
65	18.11	29.92	33.25
70	20.14	33.55	36.8

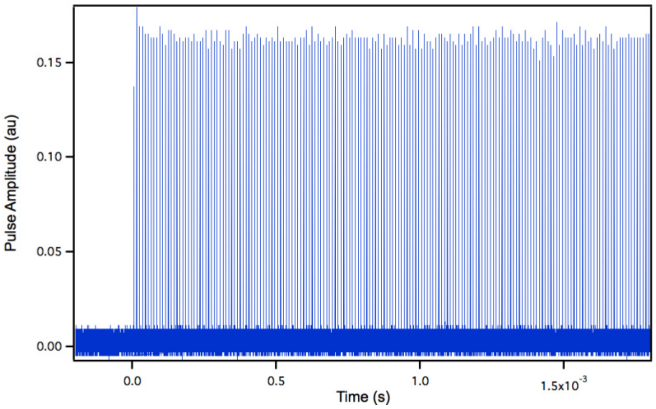

Figure 10. Measurement of single pulse energies in a super pulse over approximately 1.5 ms (of 5 ms total) at reduced energy. The output fluctuations are relatively flat, around 5% or less.

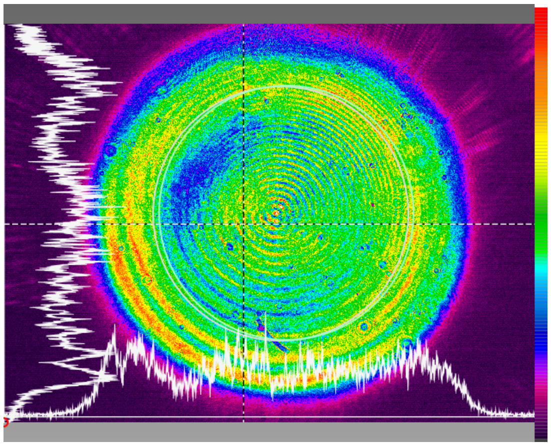

Figure 11. Spatial beam profile after amplification in the 10 mm head. At this point, the beam exhibits significant diffraction rings from the rod aperture. Thus, relay imaging or spatial filtering is required to deliver the beam to the harmonic conversion or experimental region.

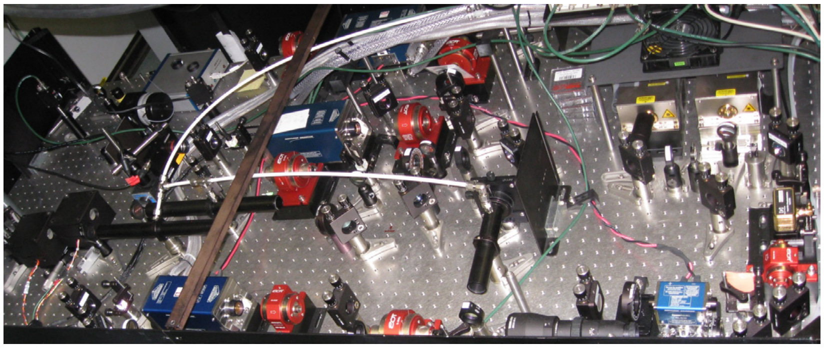

Figure 12. Photograph of the current breadboard layout showing the two seed lasers, 2-pass amp, 4-pass 5 mm amp and two 4-pass 10 mm amps.

Harmonic conversion

The output of the system is frequency converted to 532 nm with either an LBO or KTP crystal. LBO offers a higher damage threshold (18.9 GW/cm^2) than KTP (4.6 GW/cm^2), but lower nonlinear coefficient (1.05 pm/V vs. 4.35 pm/V), requiring a longer crystal to achieve high conversion efficiency. For LBO, several crystal choices are available, however we chose to evaluate a type I cut, critically phase-matched LBO crystal. Unfortunately, non-critically phase matched operation requires crystal temperatures beyond the range of our controllers. Two lengths were evaluated: a 15 mm and 20 mm length crystal. For the 15 mm crystal, we achieved approximately 30% conversion efficiency with a 35 mJ input and a 2 mm diameter beam. Since there is considerable diffraction in the beam from overfilling of the rods it was necessary to use relay imaging from the final rod amplifier to the harmonic conversion crystal.

To improve the conversion efficiency, we have also evaluated KTP which has a nonlinear coefficient approximately 4 times larger than LBO. In the non-depleted pump regime, the conversion efficiency scales as the nonlinear coefficient squared. Ultimately, we will be in the high-pump depletion region, but conversion efficiency should still be higher than LBO. The only downside is the potential for optical damage. For a 15 mm long, type I crystal, we can obtain approximately 18 mJ output at 532 nm for a 36mJ input at 1064nm. At this point, no damage has been observed, although grey tracking is known to occur over long irradiation times. The beam diameter for KTP was slightly larger than that used for LBO and was approximately 4 mm. A +500 mm focal length lens was used with a +170 mm focal length lens to image the final amp rod face onto the KTP crystal for high fidelity conversion. Since the intensities can be high in the focal regions of the lens, beam tubes with flowing nitrogen were used to reduce the probability of air breakdown and improve stability.

3. DEVELOPMENT OF METHOD FOR CORRECTING RAYLEIGH SCATTERING IMAGING MEASUREMENTS FOR EFFECTS OF LASER BEAM STEERING

Laser light scattering techniques are widely used for non-intrusive imaging measurements of reacting and non-reacting flows. In flows that have large index-of-refraction gradients, the light rays in the laser beam are refracted, causing artifacts in the recorded image that appear as stripes with either higher or lower laser light intensity. These artifacts are an impediment to quantitative interpretation of the light scattering signals. For conditions in which the beam steering is not severe and the index-of-refraction gradients are well resolved by the imaging system, a ray tracing method can be used to correct for the effects of beam steering (*3*). However, high-pressure turbulent flows have steep index-of-refraction gradients and small turbulence length scales, resulting in severe beam steering artifacts that are not well corrected using ray tracing methods.

In this project, we developed a new method of correcting for the strong laser beam steering effects that can occur in imaging of high-pressure flows. This new approach has proven very effective at removing the striped artifacts that result from beam steering while preserving the signal fluctuations due to variations in the local gas mixture or temperature. The latter fluctuations are the physical quantities that we want to measure from the Rayleigh scattering signal. The details of this new correction method will be provided in a forthcoming publication, and only a brief demonstration of the results is given here.

Figure 13a shows an example of the stripe artifacts created by index of refraction gradients in a single-shot Rayleigh scattering image of a high-pressure helium jet injected into a methane bath gas. The beam propagates from right to left in the image. This image has already been corrected for variations in the incoming beam profile using a region containing pure methane on the far right side. Variations in the incoming beam profile can result from the inherent beam profile of the laser or contaminants on the window of the pressure vessel. In experiments such as the heated pressure vessel for spray injection studies in this LDRD project (Section 5), the incoming beam profile can also have beam steering artifacts produced by index of refraction gradients in the boundary layer of the vessel window. The remaining stripes shown in Figure 13a are generated by the turbulent mixing field of helium and methane, which have disparate indices of refraction. The application of our newly developed correction method results in the image shown in Figure 13b. A comparison of Figure 13a and Figure 13b shows that this method is very effective at removing the stripe artifacts while preserving the turbulent mixing data. We tested this correction approach in the high-pressure turbulent helium/methane jet mixing experiments at a range of injection and bath gas pressures as well as using direct numerical simulations of a temporally evolving plane jet flame from E. Hawkes (*4*). In the latter case, we created a synthetic Rayleigh scattering image with and without beam steering artifacts, which were generated using a ray tracing method that related the local Rayleigh scattering signal to the index of refraction. The resulting synthetic image was then corrected for beam steering artifacts and then compared to the original image without artifacts. The errors from the beam steering artifacts were significantly reduced using our beam steering correction method. This method is used for the Rayleigh scattering measurements shown in the following sections of this report.

(a) (b)

Figure 13. Rayleigh scattering signal in a single-shot measurement of a turbulent helium gas jet injected into a methane bath gas at 8 atm. acquired using the pulse-burst laser for excitation and a high-speed CMOS camera for detection. (a) Correction for incoming beam profile only, (b) Correction for beam steering artifacts created by jet.

4. HIGH-SPEED IMAGING OF HIGH-PRESSURE GAS JET

As part of the effort to develop high-speed imaging capabilities at elevated pressure, we used a high-pressure gas-phase jet as a canonical flow geometry to provide fundamental studies of the dynamics of turbulent mixing at different pressure conditions. For this purpose, we constructed a vessel for studying transient gas-phase jets at pressures up to approximately 30 atm. A diagram of the vessel is shown in Figure 14. It consists of 6-way stainless steel cross with three flanges containing window ports. Two opposing flanges have narrow slits fitted with fused silica windows with an anti-reflection coating at 532 nm for transmission of the laser sheet from the second harmonic of the pulse-burst laser. Rayleigh scattering was collected orthogonal to the laser sheet through a circular port fitted with a fused-silica window. The fused silica was chosen for the pressure vessel windows because of its strength and to enable future UV imaging applications. An interchangeable jet nozzle was mounted on the interior base of the vessel and supplied with a burst of helium gas via a solenoid valve on the exterior of the vessel. Prior to each injection, the chamber was flushed to remove the gas mixture from the previous injection. The chamber was then pressurized with the methane bath gas to the desired pressure. For each injection, the solenoid valve was opened for 30-50 ms, depending on the pressure settings, and the 5 ms burst of laser pulses was triggered during the last 7-10 ms of the gas injection to allow time for flow transients to subside. Two injections were performed for each methane gas fill and then the chamber was vented, flushed, and refilled for the next injection. The interior surfaces of the vessel were coated with black tape to minimize background scattering, and the gases were filtered using inline particle filters as well as a cold trap to remove impurities that may condense at elevated pressures.

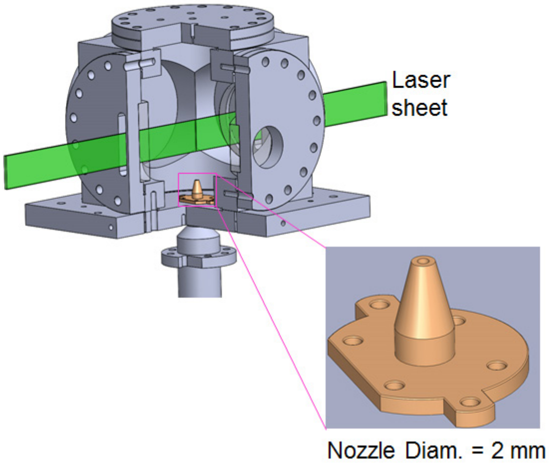

Figure 14. Pressure Vessel for Gas Jet Experiments.

The Rayleigh scattering was recorded on an unintensified high-speed CMOS camera (Phantom V2010) that was synchronized with the 100 kHz laser pulses. The images were corrected for intermittent remaining particles or condensates that were not removed by the filtering as well as for background scattering from the vessel. The background scattering was determined using a separate series of measurements with the vessel filled with either helium or nitrogen to calculate the background signal that would occur in an evacuated vessel. After background subtraction, the images were corrected for the average beam profile, throughput of the imaging optics, and camera response using a series of Rayleigh scattering images that were recorded in the pressurized methane bath gas prior to the helium injection using a separate burst of 500 laser pulses. The response-corrected images were then corrected for beam steering effects using the method demonstrated in the previous section. The fully corrected images were converted to helium mole fraction, using the uniform regions of methane on either side of the jet as the reference signal. For binary mixing in an isothermal flow, the mole fraction of the helium jet gas can be determined from the Rayleigh scattering signal, S_{Ray}, by the relation

$$X_{He} = \frac{1 - S_{Ray}/S_{Ray}^{Ref}}{1 - \sigma_{He}/\sigma_{CH4}}, \tag{1}$$

where S_{Ray}^{Ref} is the reference Rayleigh scattering signal in the pure methane bath gas and σ_{He} and σ_{CH4} are the relative Rayleigh scattering cross sections of helium and methane, respectively.

Figure 15 shows time sequences of helium mole fraction measurements from two different injection pressures. The imaged region spans 11 mm in the axial direction, centered at x/D = 21. Each sequence is a subset of the 500 shots that were recorded during a 100 kHz burst from the laser. The bath gas pressure was 8 atm., and the helium pressure upstream of the injector valve was 42 atm. and 15 atm. for the upper and lower sequences, respectively. This data enables us to resolve the dynamics of turbulent mixing, and we have performed experiments for a range of bath and injection pressures.

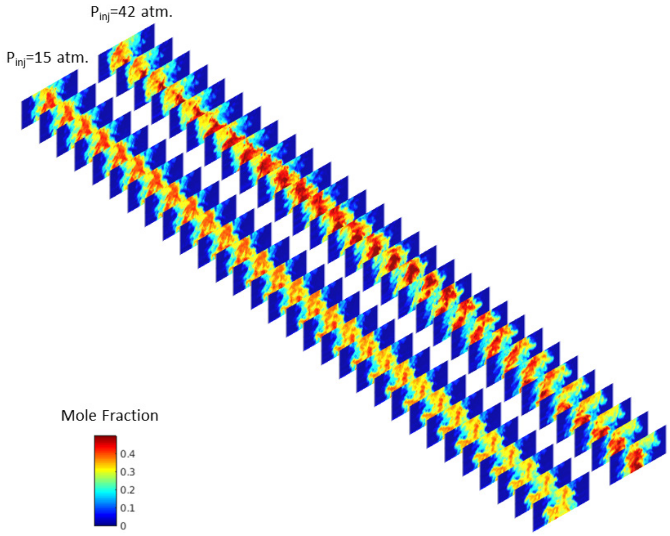

Figure 15. Time sequences of jet gas mole fraction for a helium jet injected into a methane bath gas at a pressure of 8 atm. The helium pressure upstream of the injection valve for the top and bottom image sequences is 15 and 42 atm., respectively.

Detailed analysis from these studies will be published in forthcoming journal articles, and the ability to evaluate statistics of the turbulent mixing dynamics is only briefly demonstrated here using an analysis of 84 injections for the helium injection pressure of 15 atm. and methane bath gas pressure of 8 atm., corresponding to the lower image sequence in Figure 15. For the first example, we consider the intermittency of turbulent mixing along the jet centerline. We evaluated the probability of the persistence time for a region on the jet centerline having at least 50% of its volume with a jet fluid mole fraction in the range $0.3<X_{jet}<0.5$. Figure 16 shows the resulting distribution, indicating a peak probability at short persistence times on the order of 100 us with a tail extending to milliseconds. At the peak of the distribution, there is approximately a 37% probability that 50% of the selected region of the jet has a helium mole fraction between 0.3 and 0.5 for a time period up to 200 us. This type of conditional intermittency analysis could also be used to evaluate the intermittency of ignitable regions of fuel vapor during high-pressure fuel injection. The temporal sequences of jet mole fraction measurements also enable analysis of turbulent flow time scales. In Figure 17, we show the radial profile of the integral time scale across the jet at x/D = 21. The integral time scales were determined by calculating the temporal autocorrelation from the time sequence of mole fraction measurements and integrating the autocorrelation function out to the first zero-crossing. The longest integral time scale of 250 us occurs in the outer region of the jet shear layer where methane is first entrained by the helium jet flow. On the jet centerline, the integral time scale decreases to approximately 60 us. Our new high-speed imaging capability thus enables measurements of statistics of time scales and intermittency that provide insights into the temporal evolution of the turbulent flow field and can be used for comparisons with numerical simulations. Ongoing studies will provide a detailed analysis of flow time scales under different injection conditions.

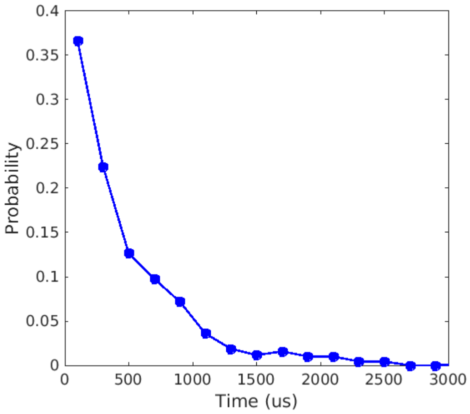

Figure 16. Intermittency measurement of a region on the jet centerline showing the probability that the local jet fluid mole fraction persists within the range $0.3<X_{jet}<0.5$ for a given time period.

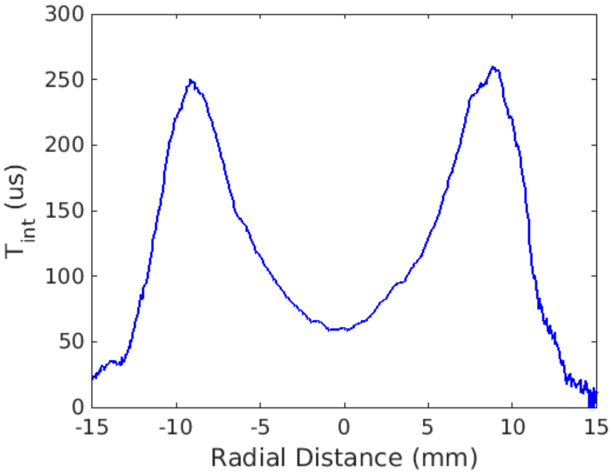

Figure 17. Radial profile of integral time scale across helium jet calculated from of 100 kHz Rayleigh scattering image sequences from 84 injections. The pressures of the methane bath gas and helium upstream of the injection valve were 8 atm. and 15 atm., respectively.

5. HIGH-SPEED IMAGING OF HIGH-PRESSURE SPRAY INJECTION

5.1. High-Pressure Spray Vessel

Experiments were performed in a constant-volume vessel under simulated conditions experienced in practical internal combustion engines. The vessel, shown in Figure 18, has internal dimensions that are cubical, measuring 108 mm on each side. The fuel injector is mounted at the center of a metal side-port such that a diesel or gasoline spray is directed into the center of the chamber. Windows located in other ports of the combustion vessel permit line-of-sight and orthogonal optical access to the injected fuel jet, including probing with a laser sheet. Further details of the combustion vessel are found at the Engine Combustion Network website (www.sandia.gov/ECN).

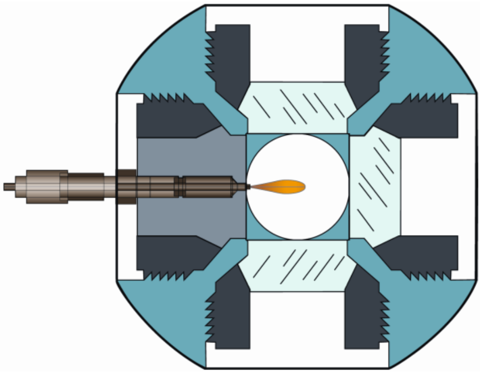

Figure 18. Optically accessible combustion vessel with fuel injection.

Engine conditions are simulated by using a premixed, combustible-gases mixture, which is spark-ignited to create a high-temperature, high-pressure environment in the vessel. Following the premixed combustion, the combustion products cool over a relatively long time (~1-3 s) due to heat transfer to the vessel walls and the vessel pressure slowly decreases. When the desired pressure and temperature are reached, the fuel injector is triggered and fuel injection occurs.

The temperature, density, and composition of the ambient gas in the vessel at the time of diesel fuel injection can be varied widely with this simulation procedure. The conditions of the ambient gas at the start of injection are determined by the initial mass and composition of gas within the vessel and the pressure at the time of fuel injection. Experiments may be performed in an inert post-preburn environment of 0% O_2, to evaluate the effects of mixing and spray vaporization without the complication of spray combustion. Table 4 shows the ambient gas composition for one of the main experimental targets, Spray A, which is a relevant and intensely studied condition for research of the Engine Combustion Network.

Table 4. Ambient gas conditions for the non-reacting "Spray A" and "Spray G" conditions.

	%vol O_2	0.00
	%vol CO_2	6.52
	%vol N_2	89.71
	%vol H_2O	3.77
	Molec. Weight MW	28.68
Spray A	Ambient temperature	900 K
Spray A	Ambient density	22.8 kg/m^3
Spray A	Vessel pressure	6.0 MPa
Spray G	Ambient temperature	573 K
Spray G	Ambient density	3.5 kg/m^3
Spray G	Vessel pressure	0.6 MPa

The Spray A fuel injector nozzle is a 0.090-mm, single-hole injector. N-dodecane is used as surrogate for diesel fuel, injected at 1500 bar. Spray G is an 8-hole (typical for current production) gasoline fuel injector with 0.170-mm holes at a drill angle relative to the injector axis of 37°. Iso-octane is used a surrogate for gasoline, injected at 200 bar. Further detail about these injectors, including the internal shape, is available on the ECN website.

5.2. Rayleigh Scattering Imaging in Spray Chamber

Rayleigh scattering provides a means to quantify atomic or molecular concentrations based on the elastic scattering of light from atoms, molecules, or particles that are small relative to the incident light wavelength. The method is effective when the Rayleigh cross-sections of the species present in the media of interest are within a few orders of magnitude of each other and background interference is minimized. If a particular component is characterized by a Rayleigh scattering cross-section that is too large, the scattered signal can show up as a small, local discontinuity in the image or may even saturate the detector locally requiring additional post-processing steps to remove such events and interpolate between neighboring unsaturated spatial locations. In severe cases charge-blooming can occur, in which saturation spreads throughout a larger region of the detector making images unusable. Consequently, successful quantitative Rayleigh scattering measurements require special care to ensure a particle-free or nearly particle-free environment. Moreover, potential sources of large molecules with very high Rayleigh cross-sections must be eliminated to prevent contamination of the probed media by species yielding light scatter outside the dynamic range of the detection system. Finally, when Rayleigh scattering measurements are performed within a closed vessel, effort is required to minimize background signal caused by reflections and laser flare from windows and other surfaces. In Figure 19, we highlight the contamination and background sources. In the sections below, we discuss the efforts undertaken in preparation for the experiments to minimize the negative impact caused by contamination and background sources.

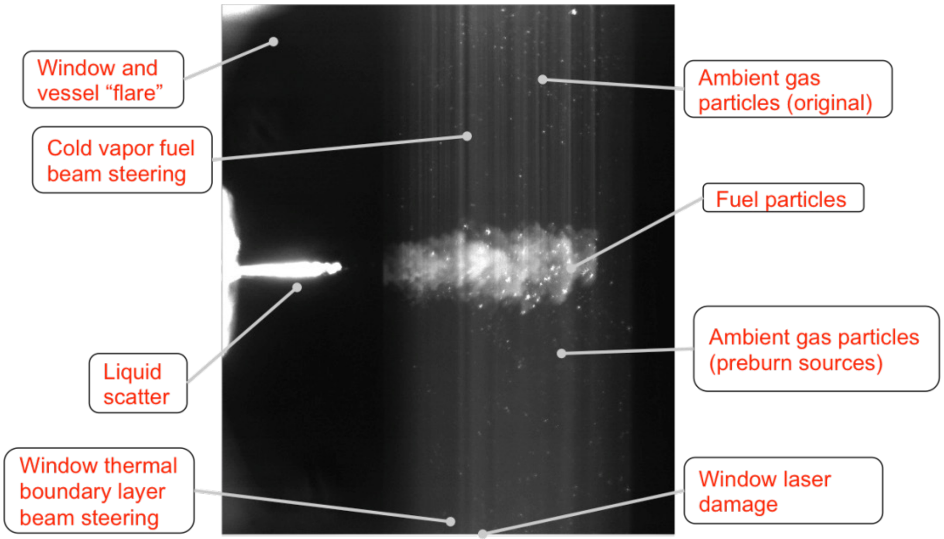

Figure 19. Single-shot image of Rayleigh scattering from a non-reacting diesel jet. The fuel (n-dodecane) was injected from a 90-µm orifice at a pressure of 150 MPa. The ambient temperature and pressure were 900 K and 6 MPa, respectively.

Window and Vessel “Flare”

Reflections and scatter from vessel surfaces and windows (referred to as “flare”) increase background signal thereby reducing the signal-to-noise ratio. To minimize flare, we developed “recessed” laser-access window “slits” as shown in Figure 20. In addition, internal non-reflective baffles are used to block flare from the window surface itself. Where possible, vessel internal surfaces are designed flat coated with a high-temperature black paint or carbon-black coating. Reflective components that cannot be painted, such as the spark electrodes, are moved to a different position away from the observation area. Because flare cannot be completely eliminated, it must be repeatedly measured in an evacuated vessel to detect changes as the experiment progresses.

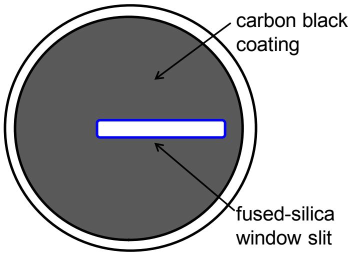

Figure 20. Metal port with fused-silica window insert (7×58 mm) for laser sheet transmission.

Beam Steering by Cold Fuel Vapor

Refractive index gradients at the boundary between hot ambient gases and cold fuel vapor cause refraction of light rays in the laser beam (i.e., beam steering). These effects are more severe at higher ambient pressures. In Figure 19, the laser passes from the bottom of the image to the top. We observe that the beam is more "striped" in the top portion of the image after passing through the cooler fuel vapor. To mitigate this effect, we developed a wavelet-based algorithm to correct for local, pixel-by-pixel laser intensity variations, from shot to shot.

Liquid Scatter

The fuel volatility, ambient temperature condition of interest, and laser position along with camera field of view can result in unwanted scatter from liquid fuel droplets. Typically, the laser is positioned sufficiently far downstream of the liquid length to avoid scatter from liquid droplets causing detector saturation.

Beam Steering by Window Thermal Boundary Layer

Steep temperature gradients at the vessel windows result in refractive index gradients and beam steering. Because such artifacts are unavoidable, correction methods are required. With a sufficiently large field of view outside the spray region, the scattering in the ambient gases can be used as reference for a built-in laser intensity correction.

Particles in Ambient Gas from Intake Gases

Particle contamination of vessel surfaces can occur during vessel servicing such as window or injector changing, seal, valve, or thermocouple replacement, or even during the cleaning process intended to remove deposits from the vessel internal surfaces. Particles may also be introduced during intake of commercial grade inert and combustible gases or when the intake manifold is pressurized prior to valve opening. Metallic particles may be generated during valve opening and/or closing as the valve poppet disengages and engages from the valve seat. Finally, heavy molecular weight species (e.g., pump oil) may condense under certain conditions. The number of particles originating in the ambient from surfaces, inlet gases, or valve opening can be mitigated as follows. Only install parts that have been cleaned of any loose debris that may be aerosolized during the intake process or pre-burn event when velocities are relatively high and particle entrainment can occur. Wipe internal surfaces with a lint-free cloth prior to installation of the final sealing window. Filter delivery gases with 3-nm filter. Ensure inlet valve opening prior to inlet manifold pressurization to ensure slow discharge. Limit heavy-oil condensates.

Fuel Particles

Historically, liquid fuels have been delivered at high pressure (up to 2500 bar) to the fuel injector by an air-driven, dual piston, liquid pump. In such a pump, both oil and seal packing material may be sources of fuel contamination. To eliminate pump contamination as a source of unwanted Rayleigh scatter, we installed a syringe pump. Use of the syringe pump significantly reduces the complexity of the fuel delivery system and can be purged and cleaned in a matter of minutes rather than hours.

The spectrophotometric grade n-dodecane used in this study was considered particle free provided contamination did not occur when transferring fuel from the original container to the fuel delivery system. Caution must be taken when using bottles taken from storage that may have dust particles deposited on the lid and bottle surface. Gloves must always be worn to both protect the person from the fuel and to protect the fuel from human contamination. To confirm the purity of the n-dodecane, samples were placed in a centrifuge and subsequently transferred to the syringe pump for Rayleigh scattering experiments. No improvement was observed in the particles observed in the spray. Therefore, it was concluded that the new untreated fuel is sufficiently clean.

Ambient Gas Particles (preburn combustion sources)

Recessed windows provide a significant improvement with regard to reducing laser flare in the high-pressure spray Rayleigh scattering experiments. Window installation requires an RTV adhesive that is normally protected from hot combustion gases by a metal cover plate. As the glue line of the recessed windows is located farther from the core of the vessel, it was assumed that high-temperature gases would not cause charring of the glue line. However, during and after the pre-burn the glue line did appear to char resulting in a particle source. A recessed window insert was designed to protect the glue line and eliminate this particles source.

Baffles fabricated from thin sheet metal and attached to the metal glue line covers are another alternative to the use of recessed windows. The metal baffles are coated with a high-temperature paint to prevent flare and specular reflections of the laser. Larger parts coated with the high-temperature paint do not reach temperatures high enough to cause the paint to break down; however, baffles fabricated from thin sheet metal appear to reach temperatures beyond the limit of the paint. As the paint degrades, the thin metal baffles also corrode over time and both appear to be sources of particles.

The standard high-pressure radial seal assembly used in this vessel includes a backing ring, a two-piece seal (body and o-ring insert), and a cover ring. Particles are easily deposited in the crevices formed within and around this assembly. All seals and associated components should be cleaned prior to installation. A newer seal design with a room temperature vulcanization (RTV) silicone filling the radial seal crevice was employed at the beginning of this study. The RTV did not perform at high temperature as anticipated and was identified as a particle source. The original seals were therefore reinstalled.

Window Laser Damage

High-power lasers easily damage low-grade or dirty windows and optics. To minimize laser damage, we used high-grade optics with AR coatings (where possible). Windows and optics must be kept extremely clean.

Rayleigh Scattering Optical Implementation

The pulse-burst laser was configured with energies of approximately 13 mJ/pulse at 532 nm, and directed into a 20 mm wide and 0.2 to 0.3 mm thick laser sheet, passing through the fuel jet centerline. The laser sheet spanned axial distances from the injector of approximately 15 mm to 35 mm. The Rayleigh scattering signal was collected using optics and high-speed camera settings given in Table 5.

Table 5. Camera and lens configurations for Rayleigh scattering imaging.

Camera	Photron SA-X2
Pixel resolution	384 × 264
Framing rate	100 kHz
Lens focal length	58 mm
Lens f/#	f/1.2
Close-up lens	500 D lens
Optical filter	532-nm center (10 nm FWHM)

Conversion to Fuel-Air Mixture Measurements

With correction for instantaneous laser-intensity fluctuations, and avoidance of scatter from liquid droplets or particle contaminants, the Rayleigh scattering signal can be shown to be proportional to the local fuel-air mixture. We emphasize that a key aspect for quantification is the ability to simultaneously measure signal from the ambient and fuel jet, as was shown in Figure 19. The measurement of the unmixed ambient just outside of the jet serves as a built-in calibration to correct for beam steering and laser intensity distribution. These laser intensity variations are clearly apparent in Figure 19. Not only is the incoming laser intensity non-uniform, but as the laser beam propagates through the vaporized fuel jet from bottom to top there is additional beam steering caused by temperature variation within the jet. However, the simultaneous measurement of a Rayleigh scattering signal from uniform ambient gases, as well as vaporized jet, provides a means for correction of beam steering and laser intensity distribution variation on a shot-by-shot basis. The description in the next several paragraphs explains how the measured intensity is converted to fuel-air ratio for a relevant engine spray condition known as "Spray A" for the Engine Combustion Network (see www.sandia.gov/ECN).

As the ambient gases surrounding the jet consist of known constituents with known Rayleigh cross-sections (see Table 6), temperature, and pressure, the Rayleigh signal from the unmixed ambient can be written as:

$$I_{R,a} = \eta I_l N_{a,o} \sigma_a \,, \tag{2}$$

where η is the signal collection efficiency, I_l is the laser intensity, $N_{a,o}$ is the number density of the ambient (outside the jet) and σ_a is the mole-fraction-weighted effective Rayleigh cross-section of the ambient (5.61 x 10^{-27} cm^2). In the vapor region of the jet, the Rayleigh scattering signal is generated by the same laser beam and from a binary mixture of the ambient and fuel vapor ($N_{mix}=N_a+N_f$) (Note that N_a is not the same as $N_{a,o}$). In the jet region, the scattered intensity is:

$$I_{R,j} = \eta I_l N_{mix} \left\lfloor X_f \sigma_f + X_a \sigma_a \right\rfloor \tag{3}$$

As $X_a+X_f=1$ and according to the ideal gas law $N_{mix}/N_{a,o}=T_a/T_{mix}$ (T_a is the ambient temperature outside the jet and T_{mix} is the temperature of the fuel-ambient mixture), dividing Eq. 3 by Eq. 2 yields:

$$\frac{I_{R,j}}{I_{R,a}} = \left(\frac{\sigma_f/\sigma_a + N_a/N_f}{1 + N_a/N_f} \right) \frac{T_a}{T_{mix}} \,. \tag{4}$$

The conservation of energy combined with the assumption of adiabatic mixing between the ambient gas and liquid fuel at known thermodynamic conditions results in the relation $T_{mix} = f(N_a/N_f)$ *(5)*. Therefore, one may solve for N_a/N_f by utilizing this functional dependence for T_{mix} in Eq. 4 and measuring the Rayleigh scattering signal from the jet and ambient gas. Converting between fuel-ambient number ratio N_a/N_f and mass ratio F/A using molecular weight, one arrives at the fuel mass fraction or mixture fraction Z

$$Z = Y_f = \frac{F/A}{(F/A + 1)} \tag{5}$$

The ratio F/A can be converted to an effective equivalence ratio ϕ using the stoichiometric F/A ratio for the fuel and ambient.

Table 6. Ambient gas and fuel vapor Rayleigh scattering cross-sections (*6*)

	N_2	CO_2	H_2O	nC7	nC12
σ_i x 10^{-27} [cm^2]	5.23	12.02	3.66	309.80	851.90

5.3. Particle Image Velocimetry in Spray Chamber

System Preparations to Perform PIV

Performing velocity measurements in a high-pressure spray environment required a number of preparatory steps. Prior to this project, PIV had never been performed in the Sandia spray chamber, and applications in chambers at high-pressure, high-temperature conditions are generally limited (e.g. Ref. (*7*)). As a first step, a custom high-pressure seeder was manufactured, tested, and installed in an intake line designed to accommodate particles. A schematic of the setup is shown in Figure 21. The design of the seeder followed a successful design generously shared by colleagues at IFP Energies Nouvelles, where a magnetically coupled rotating particle stirrer is contained within a pressure vessel. Zirconia particles of (1 µm diameter) are placed in a perforated tray and entrained by gas flowing through the tray, while mixed by the magnetic particle stirrer.

The vessel was initially filled with a combustible mixture, followed by a controlled amount of nitrogen driven through the seeder. The speed of the stirrer motor was controlled by a precision power supply and adjusted to compensate for reduction of particles in the seeder as the experiments progressed. Experiments showed that it was beneficial to add seed as the last step in the gas fill order to minimize particle deposition upon vessel walls and windows. Both the pressure upstream of the seeder, and the time of the nitrogen flow, were controlled so that the final mixture was repeatedly consistent in composition and seeding density. The composition of the initial combustible mixture was modified such that the final mixture, including the nitrogen of the seeded gas, matched the previous unseeded combustible mixture (i.e. that given in Table 4).

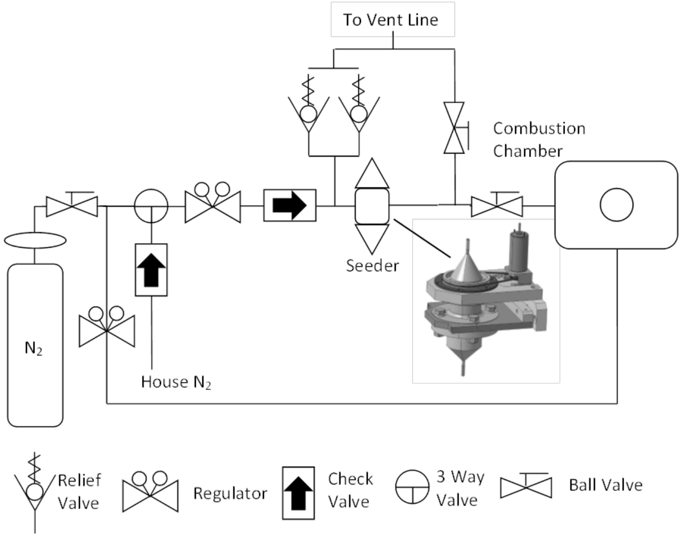

Figure 21. Schematic of high-pressure particle seeding system.

PIV Optical Setup

PIV was performed in both diesel (Spray A) and gasoline (Spray G) sprays. For Spray A, the laser sheet orientation was essentially the same as that already described for the Rayleigh scattering experiments. The setup for Spray G is shown in Figure 22. The 8-hole injector is rotated such that the laser sheet bisects different plume pairs, in particular plumes 2 and 3 on the left, and plumes 6 and 7 on the right. This arrangement avoids the strongest liquid scatter from the center of each plume, which can interfere with the PIV measurement, while probing the velocity field between plumes as shown in the figure.

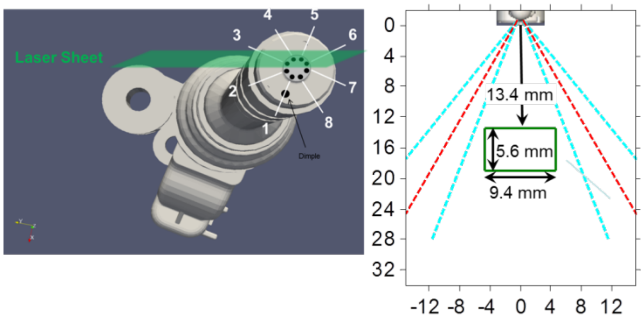

Figure 22. Optical setup for PIV experiments at Spray G conditions. The diagram at the right shows the cross section of individual plumes of the spray as dashed lines, the PIV interrogation region in solid green, and scale given in mm.

The pulse-burst laser was operated in a dual-pulse mode with pairs of laser pulses separated by 2.5 μs delivered at 100 kHz. To collect scatter from each pulse, we operated the high-speed camera at 200 kHz in a frame straddling configuration with other settings given in Table 7.

Table 7. Camera and lens configurations for PIV imaging.

Camera	Photron SA-X2
Pixel resolution	256 × 152
Framing rate	200 kHz
Frame exp. time	3.98 μs
Lens focal length	200 mm
Lens f/#	f/8
dt between pulses	2.5 μs

5.4. Results from High-Speed Imaging in Spray Chamber

Motivation for Transient Diesel Spray Mixing Experiments

Experience has shown that prediction of ignition delay and stabilization of lift-off length is a significant challenge for current CFD models. A depiction of ignition processes at Spray A conditions is given in Figure 23. A time sequence of 150 kHz Schlieren imaging from Ref. (*8*) is shown, along with corresponding simulated equivalence ratio contours from the model of Musculus and Kattke (*9*). The sequence includes several times during the cool-flame (low-temperature) ignition process up until the time of high-temperature ignition.

The first four Schlieren frames include a small annotation arc at 20 mm to highlight a region of interest where a "softening" of the Schlieren effect is eventually observed due to cool-flame heat release. At 207 μs, the region below the arc appears dark in the Schlieren image indicative of a steep density gradient at the boundary of the vaporized fuel and warmer ambient gases. At 227 μs and 234 μs, the region below the arc becomes gradually brighter suggesting that the density gradient has diminished due to a local rise in temperature resulting from cool-flame heat release. At 240 μs the region below the arc is completely transparent as the local temperature has increased further and the local density gradient is insufficient to induce a detectable Schlieren effect. In only the course of 33 μs (between 207 μs and 240 μs) while the Schlieren effect softens in the highlighted region, the head of the jet penetrates less than 3 mm downstream and the dark boundary in the Schlieren images representing the shape or structure of the penetrating spray head does not significantly change. With increasing time to 320 μs, the head of the jet also appears to "soften", indicating cool-flame heat release. The head of the jet and radial edges of the jet "reappear" by 370 μs, which is caused by a transition to high-temperature ignition, as low-density regions create strong Schlieren effects.

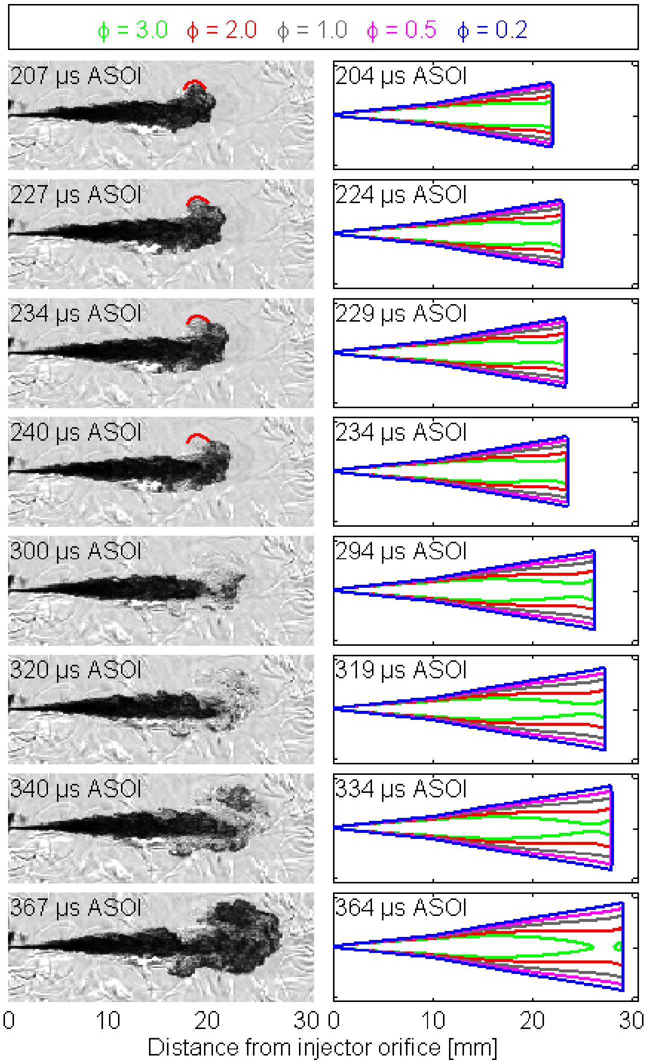

Figure 23. Time sequence of Schlieren images and corresponding model equivalence ratio contours at Spray A conditions, with 15% ambient oxygen.

The image sequence shows very fast ignition processes with multiple stages occurring downstream of 15 mm from the injector, with the head of the jet penetrating less than 30 mm. The model jet shows possible fuel-ambient equivalence ratios of these igniting regions, but direct, time-resolved measurements are needed to understand the dynamics of mixture formation and ignition. For this reason, the pulse-burst laser sheet was aligned in the critical ignition region at axial distances from 15 mm to 35 mm.

Fuel-Air Mixing Measurements in Vaporizing Diesel Sprays

An overview of a time sequence of mixing and temperature fields directly measured after application of Eqs. 2-4, along with correction for transient laser flare and beam-steering using the newly developed algorithm, are shown in Figure 24. This overview shows the evolution and mixing of jet structures, including large-scale structures at the head of the fuel jet that are shed to the side and eventually re-entrained into the fuel jet. A sharp gradient in mixture fraction exists at the head of the jet, but there is less change in mixture fraction across the width of the jet at the head compared to upstream regions where a cool, fuel-rich core exists at the spray centerline.

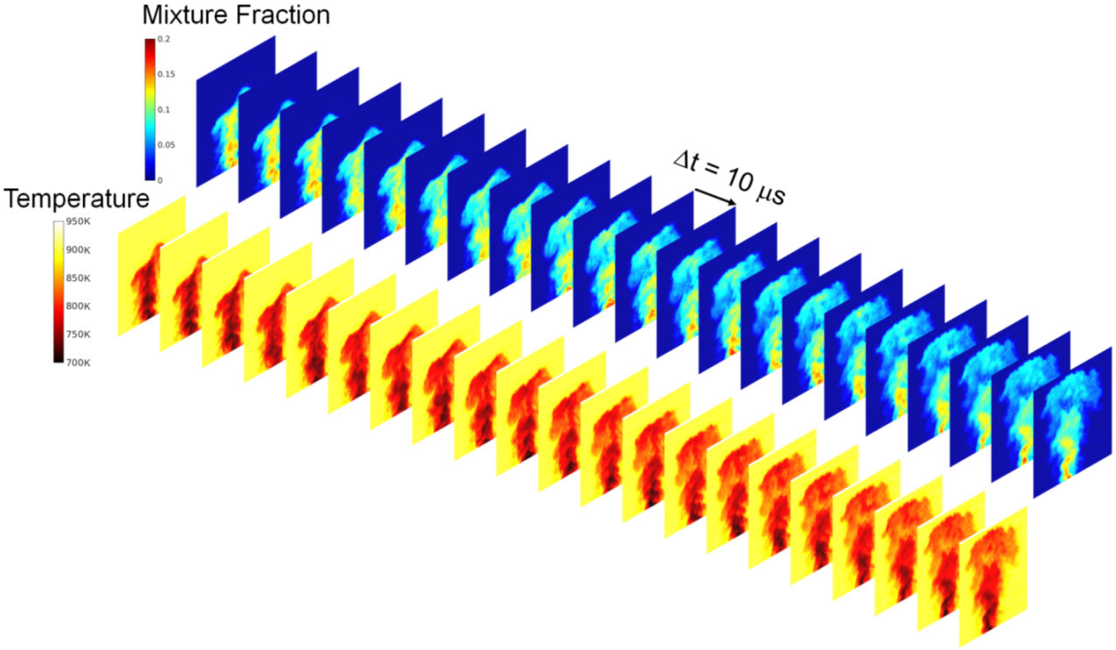

Figure 24. Time sequence (left to right) of measured mixture fraction and temperature in the ignition region of Spray A. Nozzle is at bottom and axial field of view is 17 to 35 mm.

In Figure 25, we show a time sequence of the measured equivalence ratio. Even though the mixing data were non-reacting, we compute the equivalence ratio for a reacting mixture using the same ambient gas oxygen concentration as for the ignition visualization given in Figure 23 (15% oxygen). The side-by-side comparison of mixing and ignition location shows that the first visible cool-flame ignition occurs in regions at the radial periphery of the fuel jet where the equivalence ratio is less than a value of two. Structures of significant size and uniformity appear at the radial periphery in the time period between 240 μs - 300 μs, consistent with the cool-flame heat release period where the line-of-sight Schlieren images appear to soften.

Having identified the first chemically reactive structures, we can track how these structures mix with the rest of the fuel jet leading up to high-temperature ignition. For example, the structure at the top of the jet at 300 μs is entrained back into the jet and mixes in the head region by 370 μs, when the transition to high-temperature ignition is shown in Figure 23. The high temporal resolution of the mixing diagnostic allows us to conclude with confidence that the cool flame products are mixed into the interior and head of the spray at the time of high-temperature ignition, no doubt influencing the ignition event. The sequence of mixing with structures rolling off of the head of the jet continues later in injection, yielding periods of time where there is a rather flat distribution of mixture across the head of the jet (e.g. 600 μs), but a very steep mixture gradient along the axial direction of the jet head. These mixing and ignition characteristic are key features to evaluate when analyzing predictions from various CFD approaches.

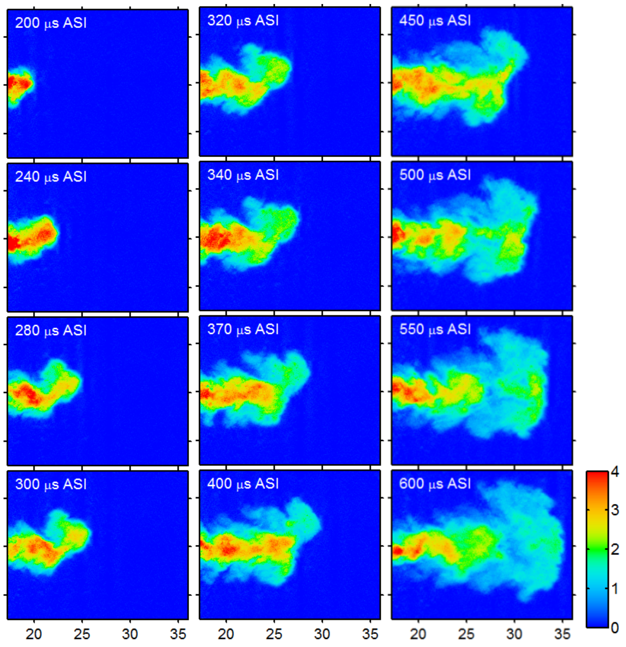

Figure 25. Equivalence ratio distribution at select timings relevant to ignition at Spray A conditions. Bottom scale is axial distance from injector in mm.

Motivation for Measurements in High-Pressure Sprays

There is a strong need for quantitative velocity information in both gasoline and diesel fuel injector sprays, and ultimately, high-speed PIV measurements were performed in both systems. To highlight this need for a target gasoline injector, Spray G of the Engine Combustion Network (see www.sandia.gov/ECN), we provide some relevant background information about the performance of Spray G in this section.

High-speed extinction imaging along a line of sight, shown in Figure 26, indicates that the spray behavior changes dramatically when the ambient gas density is varied. The plume orientation in this visualization is the same as that depicted in Figure 22, with the camera at the bottom and diffuse illumination behind the spray. In this orientation, plume pairs 1-4, 2-3, 5-8, and 7-6 are in alignment with one another, giving the perception that there are four distinct plume pairs. Each individual plume has a certain spreading angle, and is attracted to its neighbors. For the 3.5 kg/m^3 condition at the left, the plumes appear separate during injection as a clear zone is found between the 1-4 and 5-8 plume pairs. However, after the end of injection, the plumes appear to merge in the upstream region while the head of the plumes remains separate and distinct for a time downstream. With increasing time and further mixing, the liquid droplets vaporize and cause less light extinction. The "gap" between plumes can be exploited to deliver the laser sheet with less attenuation from liquid scatter for PIV imaging within the center of all plumes, as shown in Figure 26.

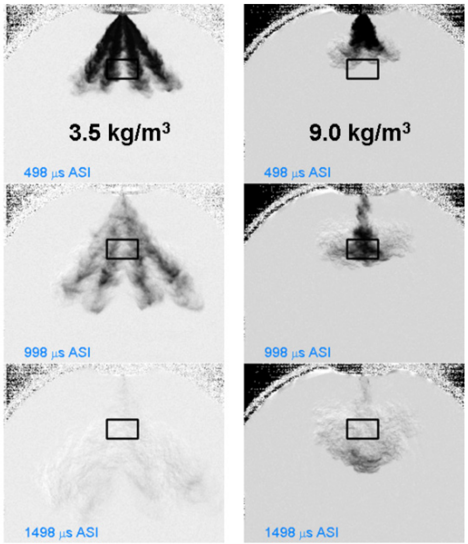

Figure 26. Comparison of line-of-sight liquid extinction for Spray G at different ambient densities. The boxed region is the position of the PIV imaging. The injection duration is 0.78 ms.

By contrast, the 9.0 kg/m^3 condition at the right indicates that plumes are in the process of collapsing together by 500 µs, and have completely merged by 1000 µs. The subsequent penetration and mixing proceeds as one collective jet, and there is higher momentum along the axial direction than any of the single plumes. The substantial difference in mixing behavior when ambient density is varied for Spray G is documented in further detail in Ref. (*10*).

The substantial shift in fuel-air mixture distribution is a major concern for engine operation. For example, the high density condition tends to produce a fuel mixture that is too rich near the center of the cylinder, and it does not use all of the air within the cylinder effectively. By this rationale, maintaining separate plumes during injection may be more effective. However, plumes that are too separate present a different challenge because a flame must travel from a single ignition point (a spark plug), but reach all plumes (all fuel). If the flame becomes isolated in a certain plume, partial-burn or misfire can occur.

Ultimately, CFD models must accurately predict these changes in fuel-air mixing over a wide engine operating envelope in order for the CFD to become a useful design tool. Understanding the root causes of the merging between plumes requires detailed information about the velocity field between plumes. In addition, the processes of mixing and combustion are highly stochastic, but even one misfire in 10,000 cycles is unacceptable. Consequently, developing an understanding of individual spray events, resolved in time, is necessary to design more robust combustion events.

Velocity Measurements in Gasoline Sprays

An illustration of the high-speed particle image velocimetry measurements between plumes is shown in Figure 27 at the lower density 3.5 kg/m^3 condition. The images show raw particle images from the boxed region given in Figure 22 at several times during and after injection. The velocity field between plumes is a critical aspect in understanding the reasons for plume merging and collapse. At 500 μs after start of injection (ASI), the velocity field shows a strong internal recirculation towards the injector tip, with increasing negative axial velocity towards the injector tip. The entrainment field between plumes creates a strong suction to pull air up towards each of the plumes. In fact, measurements show that this velocity field begins to be established even before the tip of the penetrating plumes reaches the area of interest. The figure also shows that the PIV interrogation region is obscured by neighboring plumes at the upper left and right. This obscuration is caused by liquid scatter and extinction from plumes 1 and 8, which are in between the laser sheet and the camera, as shown in Figure 22.

With increasing time after injection and very soon after the end of injection, this dominant recirculation flow field appears to stall. Axial velocities are near zero during this time period, and quite random and chaotic. Gradually, by 2000 μs ASI, higher-velocity plumes begin to merge toward the middle and a dominant positive axial velocity field establishes at the left and the right. A weak axial flow remains in the middle, but now velocities are positive downwards even along the injector axis. The velocity field continues to develop, and by 2500 μs ASI, strong axial velocities exist throughout the entire interrogation region.

This example demonstrates the utility of the pulse-burst laser and the high-speed PIV imaging system, which enable new understanding of the fuel-air mixing processes in gasoline sprays including the merging and collapse of individual plumes. The period after the end of injection when this plume collapse occurs is particularly relevant to the engine, as this time period is when spark-ignition and flame development occur. Understanding the velocity field is essential for the optimization of combustion. The velocity datasets are also now available for benchmarking of CFD models, in particular, simulations that do not currently accurately capture the velocity dynamics between plumes and the plume collapse.

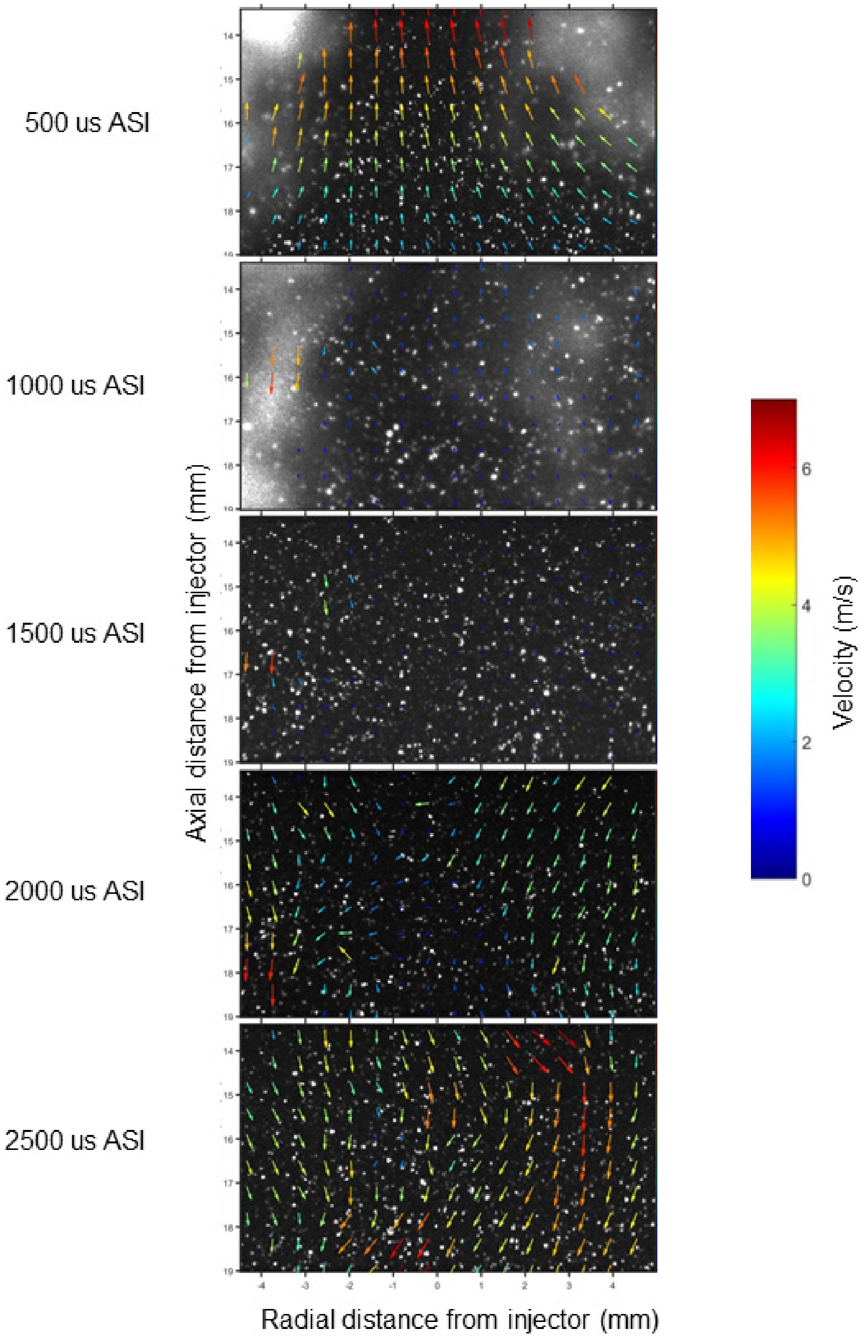

Figure 27. Time sequence of instantaneous velocity measurements overlaid on particle images at the 3.5 kg/m^3 Spray G operating condition. Time stamps correspond to time after start of injection (ASI). Every 50th shot of the 100 kHz PIV measurement is shown.

6. CONCLUSIONS

We have developed a new quantitative high-speed imaging capability that captures the dynamics of turbulent mixing in transient high-pressure flows. To attain the high data rates needed for tracking the motion of turbulent mixing in these flows, we developed a robust, mobile burst-mode Nd:YAG laser system. The laser provides 5 ms duration bursts of a 100 kHz pulse train with a burst repetition rate of order 1 Hz. We have also made significant advances in addressing the challenges of imaging diagnostics at high pressure, including the development of a method to correct for severe beam-steering effects that produce artifacts in imaging measurements as a result of steep index of refraction gradients in the flow field. This combination of developments has enabled quantitative laser scattering measurements of the dynamics of turbulent mixing during an entire high-pressure fuel injection. We demonstrated high-speed Rayleigh scattering imaging measurements of turbulent mixing in two facilities; a high-pressure gas-phase jet experiment built within this project to provide a compact, well-controlled, optically accessible, canonical flow geometry, and Sandia's constant-volume high-pressure spray facility provided liquid fuel injection at engine-relevant conditions.

In the high-pressure spray injection facility, we measured the temporal evolution of fuel mixture fraction and temperature as vaporized n-dodecane fuel mixed with high-temperature ambient gases. These measurements offer new insights into key dynamics of fuel mixture preparation in Diesel engines. We captured the re-entrainment process by which large-scale structures at the head of the fuel jet are shed to the side and eventually re-entrained into the fuel jet, affecting the ignition process. Ongoing measurements of temporally resolved mixing dynamics will permit new understanding in areas critical to the control of engine combustion. One underlying theme is the minimization of cycle-to-cycle variations, which significantly impedes engine performance with higher efficiency and lower emissions. Even 1 misfire out of 1000 cycles makes an engine unsuitable for production. However, the causes of these phenomena are not well understood. Fluctuations in the mixture preparation are thought to be a key component in these processes, and a detailed understanding of turbulent mixing dynamics in high-pressure fuel injection enabled by this research project are needed to elucidate the variations in fuel mixture.

The double-pulse feature of our burst-mode laser enabled 100 kHz particle image velocimetry measurements, which were demonstrated on a multi-plume gasoline injector. These are the first velocity measurements in Sandia's constant-volume spray injection facility. The temporally resolved velocity field imaging captured the flow reversal in the central region of the multi-plume injection, which is a key dynamic in the fuel mixture preparation for direct-injection gasoline engines. The flow reversal is linked to the collapse of the fuel plumes, in which multiple plumes merge into a single plume towards the end of injection. This collapse is particularly relevant to the engine, as this time period is when spark-ignition and flame development occur. Understanding the velocity field is essential to the optimization of combustion. The velocity datasets are also now available for benchmarking of CFD models, in particular, current simulations that do not accurately capture the velocity dynamics between plumes and the plume collapse.

This new ability to capture the movement of turbulent structures with time-resolved velocimetry will also provide a means to understand the flame stabilization phenomenon and time-history effects in Diesel fuel injection. The insight gained about Diesel flame lift-off stabilization will feed directly into CFD combustion modeling approaches. These combustion models are based on a priori assumptions about the type of physics needed to capture flame lift-off (i.e. flame propagation or ignition). Current CFD modeling practices fail in many areas, with some predicting no flame lift-off whatsoever.

In summary, this LDRD project provided a concerted experimental effort in laser diagnostics, engine research, and laser system development to provide a new capability in quantitative high-speed imaging. This new capability for high-speed planar imaging transforms our ability to study transient flow dynamics during fuel injection, and the large data rates facilitate statistical analysis. The results have broad applicability in understanding high-pressure fuel injection and other highly relevant reacting and non-reacting flows. This project has enabled experimental studies that will provide critically needed insights for Sandia's development of high-fidelity simulations of fuel injection dynamics. The experimental data will directly couple to Sandia's development of high-fidelity LES of high-pressure turbulent fluid dynamics. This coupling of quantitative measurements and numerical simulations of high-pressure turbulent flows is needed for developing advanced engine technologies.

7. REFERENCES

1. W. Koechner, *Solid-state laser engineering*. (Springer, 2013), vol. 1.
2. L. M. Frantz, J. S. Nodvik, Theory of Pulse Propagation in a Laser Amplifier. *J. Appl. Phys.* **34**, 2346-2349 (1963).
3. S. A. Kaiser, J. H. Frank, M. B. Long, Use of Rayleigh imaging and ray tracing to correct for beam-steering effects in turbulent flames. *Appl. Opt.* **44**, 6557-6564 (2005).
4. E. R. Hawkes, R. Sankaran, J. C. Sutherland, J. H. Chen, Scalar mixing in direct numerical simulations of temporally evolving plane jet flames with skeletal CO/H2 kinetics. *Proc. Combust. Inst.* **31**, 1633-1640 (2007).
5. C. Espey, J. E. Dec, T. A. Litzinger, D. A. Santavicca, Planar laser rayleigh scattering for quantitative vapor-fuel imaging in a diesel jet. *Combust. Flame* **109**, 65-86 (1997).
6. L. M. Pickett *et al.*, Relationship Between Diesel Fuel Spray Vapor Penetration/Dispersion and Local Fuel Mixture Fraction. *SAE Int. J. Engines* **4**, 764-799 (2011).
7. L.-M. Malbec, G. Bruneaux, Study of Air Entrainment of Multi-hole Diesel Injection by Particle Image Velocimetry - Effect of Neighboring Jets Interaction and Transient Behavior After End of Injection. *SAE Int. J. Engines* **3**, 107-123 (2010).
8. S. Skeen, J. Manin, L. M. Pickett, Visualization of Ignition Processes in High-Pressure Sprays with Multiple Injections of n-Dodecane. *SAE Int. J. Engines* **8**, 696-715 (2015).
9. M. P. B. Musculus, K. Kattke, Entrainment Waves in Diesel Jets. *SAE Int. J. Engines* **2**, 1170-1193 (2009).
10. L. M. Itani, B. Gilles, L. Hermant, C. Schulz, Investigation of the Mixing Process and the Fuel Mass Concentration Fields for a Gasoline Direct-injection Spray at ECN Spray G Conditions and Variants. *SAE*, 2015-2001-1902 (2015).

DISTRIBUTION

1	MS0899	Technical Library	9536 (electronic copy)
1	MS0359	D. Chavez, LDRD Office	1911 (electronic copy)

Sandia National Laboratories